Aerodynamic Design of a Rectangular Wing in Subsonic Inviscid Flow by Surrogate-Based Optimization

Xiaosong Du[1], Anand Amrit[2], Andrew Thelen[3], and Leifur Leifsson[4]
Iowa State University, Ames, Iowa 50011

Yu Zhang[5], and Zhong-Hua Han[6]
National Key Laboratory of Science and Technology on Aerodynamic Design and Research,
School of Aeronautics, Northwestern Polytechnical University, Xi'an, 710072, P. R. China

Slawomir Koziel[7]
Engineering Optimization & Modeling Center, Reykjavik University, Menntavegur 1, 101 Reykjavik, Iceland

The paper presents results of aerodynamic design of a rectangular wing in subsonic inviscid flow using surrogate-based local and global search algorithms. The aerodynamic design problem is formulated in Benchmark Cases 3 and 6 developed by the AIAA Applied Aerodynamics Discussion Group. Both involve lift-constrained drag minimization at a Mach number of 0.5 with relatively low lift coefficients (0.2625 and 0.375) with several nonlinear constraints and a small number design variables (up to 11). In this work, the local search is performed using variable-fidelity modelling and output space mapping, whereas the global search is performed using approximation-based surrogates. The paper presents the details of the computational modelling, shape parameterization, optimization algorithms, and results for each benchmark case. The approaches yield comparable results for Benchmark Case 3. Only the local search algorithm is applied to Benchmark Case 6. The results indicate the multimodality of that design case.

Nomenclature

C_D	=	drag coefficient, [-]
C_M	=	pitching moment coefficient, [-]
C_L	=	lift coefficient, [-]
c	=	low-fidelity model output vector
c	=	chord length, [m]
f	=	high-fidelity model output vector
l	=	lower bound, [-]
M_∞	=	Mach number, [-]
t	=	airfoil thickness, [m]
u	=	upper bound, [-]
V	=	wing volume, [m³]
x	=	design variables, [-]
α	=	wing angle of attack, [deg]
δ	=	trust region radius, [-]
γ	=	wing twist distribution, [deg]

---

[1] Graduate Student, Department of Aerospace Engineering, Student Member AIAA.
[2] Graduate Student, Department of Aerospace Engineering, Student Member AIAA.
[3] Graduate Student, Department of Aerospace Engineering, Student Member AIAA.
[4] Assistant Professor, Department of Aerospace Engineering, Senior Member AIAA.
[5] PhD candidate, Department of Fluid Mechanics, Youyi West Road No. 127, P.O. Box754, Student Member AIAA.
[6] Professor, Department of Fluid Mechanics, Youyi West Road No. 127, P.O. Box754, Member AIAA.
[7] Professor, School of Science and Engineering, Senior Member AIAA.

I. Introduction

This paper presents the results of solutions to the benchmark aerodynamic design Cases 3 and 6 (aerodynamic design of a rectangular wing in subsonic inviscid flow) developed by the AIAA Applied Aerodynamics technical committee. The original version of the problem (Benchmark Case 3) has the objective of minimizing the drag coefficient by optimizing the twist distribution of the wing at a fixed lift coefficient. A new version of the problem (Benchmark Case 6) will also be solved. In this version, a lift-constrained drag minimization is performed by varying the span, sweep, dihedral, chord, and airfoil shape. In addition, non-linear constraints are applied to planform area, internal volume, root bending moment, thickness, and angle of attack. The results are presented in a special session at the annual AIAA Aviation 2017 conference.

In our prior work[1,2], we attempted to solve the benchmark cases using approximation-based surrogates[3,4] (SAO) and physics based surrogate techniques[5]. In our first paper[1], we used multi-fidelity optimization with the space mapping[6] (SM) technique to solve the problem. When using SM, an unstructured 15.5M cell mesh was used as the high-fidelity model, while a VLM code served as the low-fidelity one. When using SAO, only the 15.5M cell mesh was used. Using both optimization methods, we observed drag reductions of just over one count. This drag reduction value is consistent with numerous other papers, which used varying parameterization, grid generators, flow solvers, and optimization methods. In the second paper[2], we attempted to solve the cases using the multi-level optimization[7] technique. In our solutions, we used a family of low-fidelity models and the Stanford University Unstructured[8] (SU[2]) solver to optimize a high-fidelity model by the same grid generator and flow solver as the low-fidelity models but with a higher mesh resolution (fully grid-independent solutions). In the third paper[9], we attempted to solve the problem using multi-fidelity techniques and improved computational models along with a new correction technique. The paper demonstrated that multi-fidelity optimization with physics-based models can solve the aerodynamic cases much faster than direct optimization with adjoint sensitivity information (see, e.g., Jameson[10]), and surrogate-based optimization[2] (SBO) with data-driven surrogate models[3]. The second case was introduced very recently. Thus, no information about the optimal wing shapes is currently available.

In this work, we use an updated aerodynamics model with minor modifications to the optimization methods. The unstructured mesh generator (SUMO) is replaced by separate codes that generate the solid model and structured mesh, respectively. In addition, the flow solver (SU2 version 4.0.0) has been updated to a newer version (version 5.0.0), which may have minimal effects on the result. Using a simplified set of designable geometry, this version of the problem is also solved using the two approaches. The multi-modality of this problem is investigated using multi-start local search with physics-based surrogates as well as global search with approximation-based surrogates and infill.

The paper is organized in the following way. Section II focuses on Benchmark Case 3 giving the problem formulation, details of the computational modeling and parameterization, optimization methodology, and results. Section III is focused on Benchmark Case 6 and has the same layout as Sect. II. The paper ends with conclusion.

II. Benchmark Case 3: Rectangular Wing Twist Optimization

The goal of this first problem is to minimize drag of a rectangular wing at a fixed lift by adjusting the span-wise distribution of twist angle about the trailing edge. The purpose of this is to show that the span loading of the optimized wing is approximately elliptical, which, for an inviscid subsonic case, corresponds to theoretical minimum drag and a span efficiency factor of one.

A. Problem Formulation

At a Mach number of $M_\infty = 0.5$, minimize the drag coefficient (C_D) by changing the twist distribution (γ) of an unswept rectangular wing with constant-span (b), constant-chord (c), and constant-section (NACA 0012) at a fixed lift coefficient of 0.375 (C_L) with a constraint on the twist distribution on the tip. In particular, the optimal design problem formulation is as follows:

$$\min_{\mathbf{l} \leq \mathbf{x} \leq \mathbf{u}} C_D(\mathbf{x}), \tag{1}$$

subject to

$$C_L(\mathbf{x}) = 0.375, \tag{2}$$

$$\left. \frac{d\gamma}{dy} \right|_{y=3c} \geq -10^\circ / c, \tag{3}$$

American Institute of Aeronautics and Astronautics

where **x** is the vector of design variables, **u** and **l** are the vector of upper and lower bounds of the design variables, respectively, and *y* is the coordinate along the wing span (cf. Fig. 1). The baseline geometry is shown in Fig. 1.

B.   Computational Modeling and Parameterization

In order to evaluate the loads on a particular wing design, a MATLAB-based aerodynamics model executes several sequential steps. First, the design variables are converted to the span-wise geometric distributions (e.g. twist, chord, sectional shape) using B-spline parameterization. Then, using the resulting geometry, an Engineering Sketch Pad (ESP) script is executed to produce the solid model. This CAD model is then used by a Pointwise script, which generates a structured mesh with an O-type topology. Then, SU2 version 5.0.0 is used to solve the Euler equations on the grid at the specified Mach number. Finally, MATLAB and Tecplot are used to process the results.

For the first problem considered, the particular B-spline parameterization uses three control points (shown in Fig. 2), where the center point can move horizontally and vertically, and the tip control point can move vertically. While the root twist angle is fixed at zero, each design evaluation adjusts the angle of attack to produce the prescribed lift coefficient. For each design evaluation, this is done implicitly within the flow solver.

Before initiating the optimization process, a grid convergence study was carried out for the baseline design. An initial mesh was selected having an off-wall spacing of 0.004, 100 cells along the span, approximately 170 cells around the airfoil sections, and 100 cells between the wing and far-field surface, which is located at a radius of 50. In total, the mesh has approximately 1.7M cells. Figure 3 shows the resulting surface mesh on the wing surface as well as the symmetry plane.

A set of refinement factors, ranging from 0.25 to 1.75, in increments of 0.25, was chosen. For each refinement factor value, the off-wall spacing is divided by the factor, while the numbers of cells (along wing, around airfoil, between wing and far-field) are each multiplied by the factor. The resulting meshes had numbers of cells ranging from approximately 25,000 to 9M cells. Figure 4 shows the results of this study.
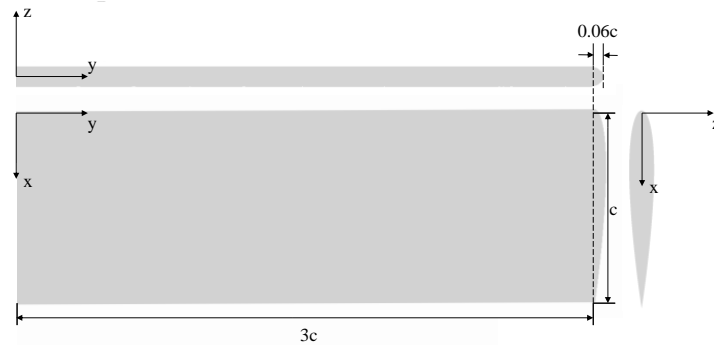

Figure 1. Baseline semi-span wing geometry for Benchmark Case 3. The wing has a constant section profile, the NACA 0012, and the tip is rounded.
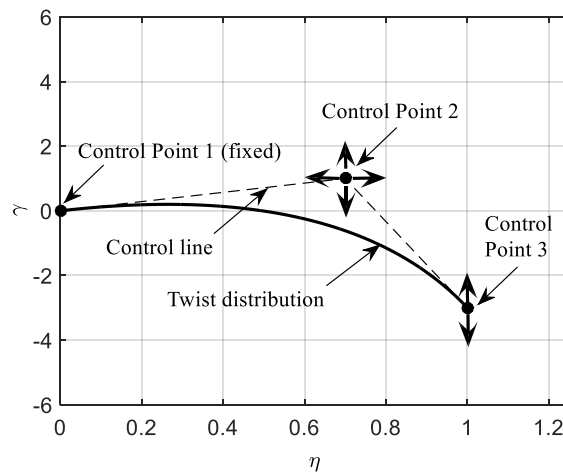

Figure 2. Wing twist distribution parameterized using a B-spline curve with three control points.

3
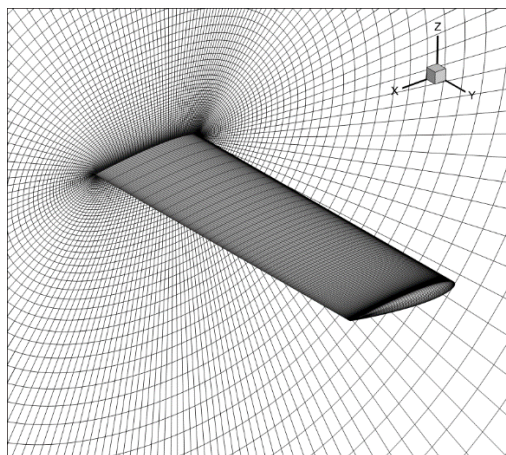American Institute of Aeronautics and Astronautics

Figure 3. Sample mesh used for the computational fluid dynamics simulations.
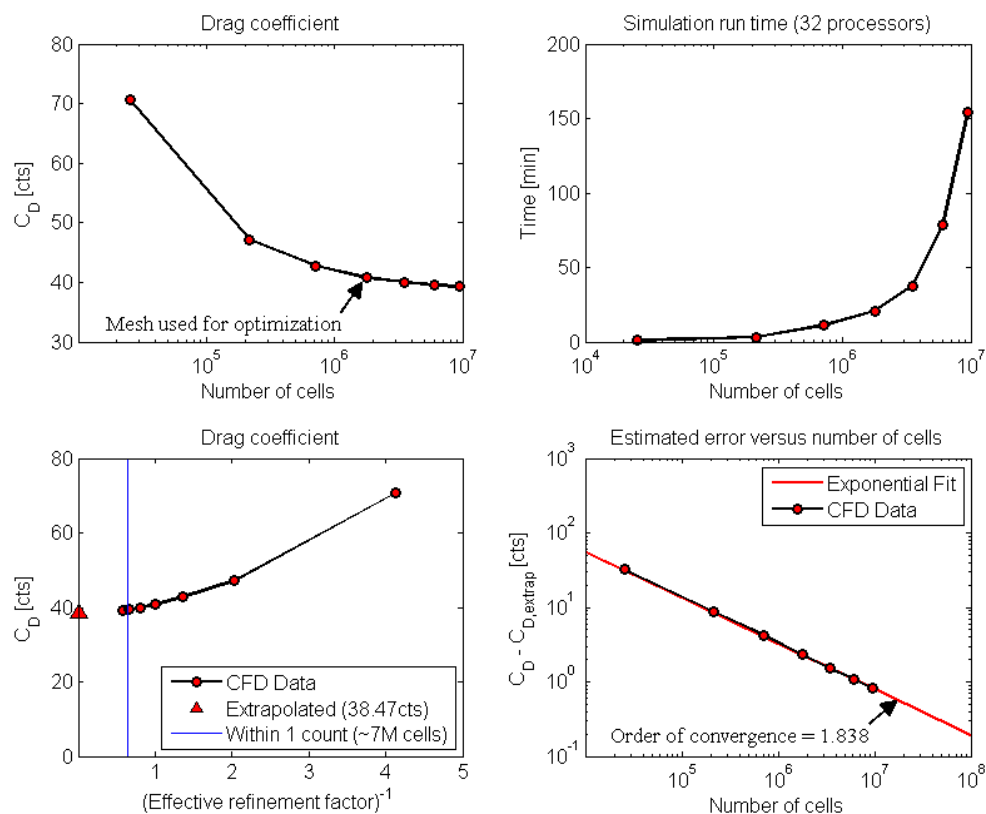

Figure 4. Grid convergence results for the baseline design at $M_\infty = 0.5$ and $C_L = 0.2625$: drag coefficient versus number of mesh cells (top left), simulation run time using 32 processors versus number of mesh cells (top right), drag coefficient as a function of the inverse refinement factor, which is computed as $\left(N/N_{ref}\right)^{1/D}$, ($N$ is the number of cells, $N_{ref} = \sim 1.7M$ is the reference number of cells, and $D = 3$ is the number of physical dimensions) (bottom left), and estimated drag coefficient error as a function of number of cells (bottom right).

In Fig. 4, the top left plot shows the resulting drag coefficient versus the number of cells, where the lift coefficient is fixed at 0.2625 (the value prescribed for Benchmark Case 6 (cf. Sect. III)). The reference mesh is indicated as well. This mesh is chosen for the optimization process because the drag coefficient is within 1 count of the drag computed using the next finest mesh. The top right plot shows the resulting run time of each simulation, where 32 processors are used for each simulation. The bottom left plot shows the drag compared to the inverse of

American Institute of Aeronautics and Astronautics

the effective refinement factor, which is computed as $(N/N_{ref})^{1/D}$, where N is the number of cells, N_{ref} is the reference number of cells, and $D=3$ is the number of physical dimensions. In this plot, the extrapolated drag value for an infinitely fine mesh (in this case 38.5 drag counts), which was found using Richardson extrapolation[19], is indicated as well. The same method estimates that a 7M cell mesh is required if an error of 1 drag count is needed. Finally, the bottom right plot shows the error of each mesh, and also provides the exponential fit used in the extrapolation process.

C. Global Search by Approximation-Based Surrogates

A typical global SBO approach, named efficient global optimization (EG[11]) method is used in this work. The EGO, proposed by Jones *et al*., includes two stages: first, a kriging model is built based on the initial sample points randomly selected by design of experiments (DoE[12]) techniques and corresponding responses calculated by numerical simulations; second, the kriging model is repeatedly updated by a specific infill sampling criterion, expected improvement (EI[11]), until the optimum is obtained. The EI criterion assumes that there is a normal distribution at each site; meanwhile the response and the mean squared error predicted by surrogate model serve as the mean value and the standard deviation. EI function is defined as the mathematical expectation of improvement at an arbitrary site, compared to the optimal solution observed so far. The EI method is well-known for its capability of balancing the need between global exploration and local exploitation of the response surface; as a result, the EGO method is quite efficient.

The optimization algorithm is performed on an in-house optimization platform named "SurroOpt[13]", shown in Figure 5. SurroOpt has built-in modern DoE well suited for computer experiments, such as Latin hypercube sampling (LHS), uniform design (UD) and Monte Carlo design (MC), and we use Latin hypercube sampling (LHS) here. A variety of surrogate models were developed such as quadratic response surface model (PRSM), kriging, gradient-enhanced kriging (GEK) [14], Cokriging[15], hierarchical kriging (HK) [16], radial-basis functions (RBFs), support vector regression (SVR), etc. Several infill sampling criteria[17] and dedicated constraint handling methods were implemented, such as minimizing surrogate prediction (MSP), and minimizing lower confidence bounding (LCB), maximizing expected improvement (EI), maximizing probability of improvement (PI), and maximizing mean squared error (MSE). In our study, the infill criterion refers to maximizing the constrained expected improvement (EI). The corresponding sub-optimization is done by combining a genetic algorithm (GA) with local optimization, such as Hooke and Jeeves pattern search, quasi Newton's methods (BFGS) and sequential quadratic programming (SQP). The iteration terminated condition of EGO is

$$\left\| x^{(i+1)} - x^{(i)} \right\| < \varepsilon_1 \text{ or } N \geq N_{\max}, \tag{4}$$

where $N_{\max}$ is the user-specified maximal number of CFD evaluations, and $\varepsilon_1 = 1e-10$. When no new samples can be found, or the number of samples reaches the maximum, the round of optimization terminates.
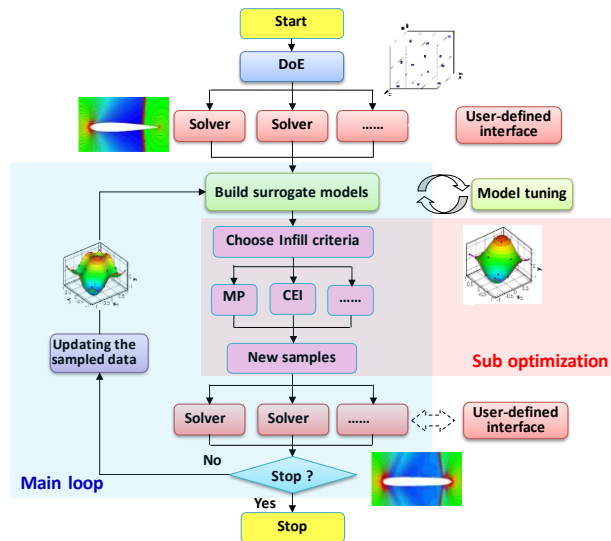

Figure 5. Framework of surrogate-based optimization in SurroOpt[13].

D. Local Search by Physics-Based Surrogates

A local multi-start search is performed using physics-based surrogate models constructed using variable-fidelity models and output space mapping[6] (OSM), where the sub-optimization processes are controlled using a trust-region framework. OSM is applied to four different response values from the high- and low-fidelity models. These include the drag coefficient, root bending moment coefficient, angle of attack, and the internal volume. When using the high-fidelity model, the first three values are computed by SU2, while the volume is computed when generating the solid model using ESP.

The low-fidelity models used in the study are of two types: a variable-fidelity physics model (simplified physics model) using a vortex lattice method (VLM), and a variable-resolution model (same governing physics but reduced discretization) using a coarse mesh and reduced flow solver convergence criteria. The VLM model computes the drag coefficient and angle of attack directly, as well as supplying the span loading, which is subsequently used to compute the root bending moment coefficient. In addition, the internal volume is computed analytically by integrating cross-sectional area across the span. Meanwhile, the planform areas for both the high- and low-fidelity models are computed analytically by projecting the wing geometry onto the XY-plane. While only the drag coefficient is important in the first case, the second case in Sec. (III) uses all of these space-mapping-corrected values for both the objective function as well as the nonlinear constraints.

Four stopping criteria are implemented for the local search based on the design variable vector ($\|(\mathbf{x}^{(i)}-\mathbf{x}^{(i-1)})/(\mathbf{u}-\mathbf{l}))\|$<1E-3), trust region size (R_{TR}<1E-4), surrogate model resolution ($|\mathbf{s}(\mathbf{x}^{(i)})-\mathbf{f}(\mathbf{x}^{(i)})|$<1E-4), and change in objective function ($H(\mathbf{x}^{(i)}) - H(\mathbf{x}^{(i-1)})$<1E-2). In addition, the maximum number of iterations is set to N_{max} = 20.

E. Optimization Results

Evolution of the objective functions of the optimization algorithms are given in Fig. 6. The local algorithm, shown in Fig. 6(a), is utilized with the two different low-fidelity models, which use different physics and different mesh resolution, respectively. When using OSM with different physics (VLM with Euler), the optimization requires three design iterations, but appears to go directly to the optimum during the first iteration. The variable-resolution approach (Euler with fine and coarse meshes) required 5 design iterations, shows better convergence characteristics, but quadrupled the optimization cost and produced a slightly worse design. The global search algorithm, shown in Fig. 6(b), required 24 design iterations using a slightly coarser mesh having approximately 216,000 cells, compared to 1.7M cells used in Fig. 6(a). For this approach, fifteen sample points generated by LHS are used to build the initial kriging model. Then, 9 sample points are chosen by EI method to update the kriging model. The twist and lift distributions of the baseline and optimized designs are given in Fig. 7. It can be seen that all of the approaches yield nearly elliptical lift distributions. Table 1 gives a comparison of the numerical values for those distributions. Table 2 gives the details of the performance of the baseline and optimized shapes, as well as the computational cost.
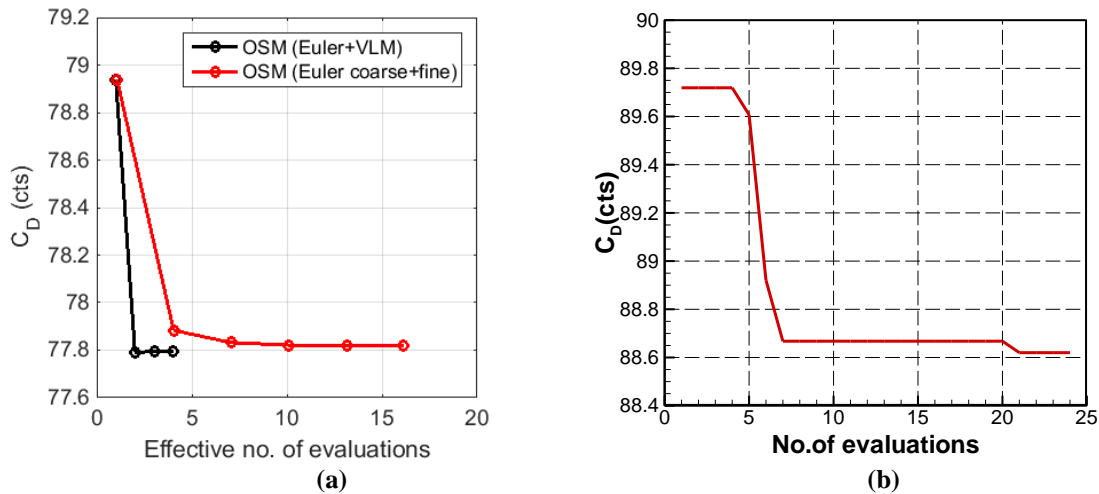

Figure 6. Optimization convergence histories of objective function: (a) runs with output space mapping, and (b) runs with SurroOpt.
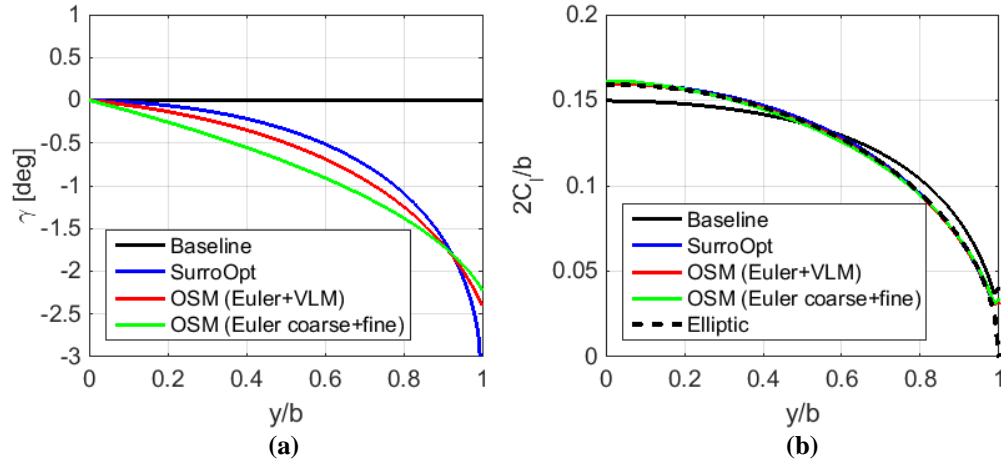
American Institute of Aeronautics and Astronautics

Figure 7. Results for Benchmark Case III: (a) the initial and optimized twist distributions, (b) resulting lift distributions.

Table 1. Comparison of twist and lift distribution of the baseline and optimized wings, where $\eta = y/b$ ($M_\infty = 0.5$, $C_L = 0.375$).

	η	0.0	0.2	0.4	0.6	0.8	0.9	0.95	1.0
Baseline	γ (deg)	0.0	0.0	0.0	0.0	0.0	0.0	0.0	0.0
	$2C_l/b$	0.1497	0.1478	0.1418	0.1294	0.1037	0.0791	0.0594	0.0387
SurroOpt	γ (deg)	0.0000	-0.0622	-0.2159	-0.5128	-1.0865	-1.6197	-2.0605	-3.3418
	$2C_l/b$	0.1599	0.1569	0.1470	0.1284	0.0953	0.0683	0.0494	0.0306
OSM (VLM+Euler)	γ (deg)	0.0000	-0.1329	-0.3482	-0.6872	-1.2445	-1.6853	-1.9881	-2.4000
	$2C_l/b$	0.1598	0.1563	0.1455	0.1265	0.0942	0.0683	0.0499	0.0312
OSM (Euler coarse+fine)	γ (deg)	0.0000	-0.2562	-0.5521	-0.9089	-1.3777	-1.7024	-1.9174	-2.2222
	$2C_l/b$	0.1609	0.1566	0.1448	0.1257	0.0943	0.0691	0.0508	0.0320
Elliptical	$2C_l/b$	0.1592	0.1559	0.1459	0.1273	0.0955	0.0694	0.0497	0.0000

Table 2. Benchmark Case 3 optimization results: attributes of the baseline and optimized wings, as well as the optimization costs.

Parameter	Baseline	SurroOpt	OSM (VLM+Euler)	OSM (Euler coarse+fine)
α (deg)	4.3157	4.8009	4.8730	5.0137
C_L (cts)	37.5002	37.5005	37.5006	37.5006
C_D (cts)	78.94	77.77	77.79	77.82
e	0.9451	0.9593	0.9591	0.9587
N_c*	–	24	95	160
N_f	–	1**	4	6
$N_{f,eq}$	–	4.41	4.03	16.14
t_c (hr)	–	1.19	0.01	3.50
t_f (hr)	–	0.35	1.44	2.07
t_{tot} (hr)	–	1.54	1.45	5.57

*SurroOpt uses a coarse mesh with ~ 216k cells, whereas the OSM coarse mesh has ~77k cells.
**SurroOpt uses a coarse mesh for optimization, then runs the fine mesh at the optimum.

III.   Benchmark Case 6: Multimodal Subsonic Inviscid Optimization

Benchmark Case 6 focuses on the same flow conditions and baseline wing design used in the previous problem, although both rounded and pinched wing tip shapes are acceptable. However, the design space is expanded to include span, chord, dihedral, sweep, and airfoil shape, making the design space more complicated and no longer convex. In addition, nonlinear constraints are introduced to enforce minimum values of volume and thickness, a maximum root bending moment, and a target planform area. This introduces further challenges when finding local or global minima. As such, the purpose of this problem is to locate an unknown number of local minima in hopes of uncovering unintuitive solutions.

Following the previous section's organization, the current section will begin with a problem description in Sect. III.A. Here, the geometry, objective function, constraint functions, and geometric limitations (i.e., bounds) of the design space will be described. Then, details on modeling and parameterization will be provided in Sect. III.B. Section III.C discusses optimization methodology that was not needed for the previous problem, and focuses particularly on how local optimization is applied on a global scale. Finally, Sect. III.D presents the optimization results.

A.   Problem Formulation

The objective of this problem is to minimize drag of a wing in inviscid subsonic flow, where the flow conditions are consistent with the previous case. While this problem allows for higher flexibility, we consider our designable geometry to be span, as well as the span-wise distributions of twist, chord, and dihedral. Although the distributions of sweep and airfoil shape are allowed to change in the problem, we fix them to zero center-chord sweep and the NACA 0012 airfoil shape. This is due to the presumption that span, chord, twist, and dihedral will allow for most of the possible drag reduction while also displaying the multi-modality of the problem. However, our investigation into this is ongoing.

In addition, we enforce six nonlinear constraints: one equality and five inequality. The equality constraint ensures a lift coefficient of 0.2625, and is enforced implicitly within the flow solver. The first inequality constraint ensures that planform area remains within 1% of the baseline value of 3.06, while the second ensures that the internal wing volume is greater than or equal to that of the baseline. The third inequality constraint limits the bending moment exerted on the wing root, where the maximum value is 0.1069 when using 3.06 as both the reference length and reference area. Lastly, the angle of attack is limited to a range of -3° to 6°. In addition, the original problem enforces a minimum thickness throughout the span, but we disregard this due to the fixed airfoil shape throughout the wing.

In particular, the optimal design problem formulation is as follows:

$$\min_{\mathbf{l} \leq \mathbf{x} \leq \mathbf{u}} C_D(\mathbf{x}), \tag{5}$$

subject to

$$C_L = 0.2625, \tag{6}$$

$$100 \left(\frac{|S_0 - S|}{S_0} \right) - 1\% \leq 0, \tag{7}$$

$$100 \left(\frac{V_0 - V}{V_0} \right) \leq 0, \tag{8}$$

$$100 \left(\frac{C_{M_x} - C_{M_{max}}}{C_{M_{max}}} \right) \leq 0, \tag{9}$$

$$-3^o - \alpha \leq 0, \tag{10}$$

and

$$\alpha - 6^o \leq 0. \tag{11}$$

Here, we represent the volume, area, and moment constraints as percentages of the reference values, which, respectively, are the minimum volume (0.24818), target planform area (3.04110), and the maximum moment coefficient value (0.1069).

B.   Computational Modeling and Parameterization

The computational models used in Benchmark Case 6 are described in Sect. II.B. In this case, however, the wing shape is described using the distributions of chord, z (vertical) coordinates of the quarter-chord locations at each spanstation, and the twist distribution, as well as the wing semi-span. Figure 8 shows the implementation of those distributions using B-spline curves (similar as described in Sect. II.B). For all of the distributions shown in Fig. 8, the horizontal coordinates of each center control point can vary between 0.2 and 0.8. For chord, the vertical coordinates of the root and tip control points can vary between 0.45 and 1.55, while the center point can vary between 0.1 and 1.9. For z-coordinates, the tip control point can vary between -0.45 and 0.45 vertically, while this range for the center point is -0.8 to 0.8. Finally, for twist, the tip control point can vary between -3.12 and 3.12 vertically, while the center point can vary from -5 to 5. Nonlinear constraints are enforced to ensure that each of these distributions fall within the ranges [0.45 1.55], [-0.45 0.45], and [-3.12 3.12] for chord, z-coordinates, and twist angle, respectively.

C.   Local Search by Physics-Based Surrogates

The output space mapping approach used in the previous case was slightly modified for the new case. In the previous case, our OSM framework was driven exclusively by MATLAB's fmincon optimization code using the SQP algorithm. However, for the current case, some difficulty was encountered when enforcing the constraints (particularly the bending moment constraint), as the SQP algorithm works well for objective function minimization but often yields infeasible designs. Conversely, MATLAB's patternsearch algorithm is more costly but always yields feasible designs, assuming the feasible space can be located. For this reason, we used a combination of the two optimizers when optimizing the surrogate model, leading to a greatly increased number of low-fidelity function calls. However, because a VLM code is used as the low-fidelity model, a large number of function calls was not a concern.

The local optimization algorithm was ran from 26 different initial designs around the design space; the first is the baseline design, while the other 25 were generated using Latin Hypercube Sampling (LHS). In order to avoid excessive clustering of the sampling plan, the LHS was optimized using the Morris-Mitchell space filling criterion, following Ref. 18. Moreover, the sampling plan initially had 100 different designs, but was filtered such that the planform area of all LHS designs were within ~6.5% of the baseline value. This percentage was varied manually until there were 25 designs in the filtered set of points. The target of 25 designs was selected based on the estimated total cost of all optimization processes.

D.   Optimization Results

After running the optimization algorithm from all 26 initial designs, four results were selected based on uniqueness and feasibility (constraints ≤1%) of the optimized design. In addition, we selected only the cases that yielded designs with lower drag than the baseline shape (~40.8 drag counts). From this point forward, we will refer to the four starting points for these optimization runs as x_1 through x_4, while the optimized designs will be referred to as x_1* through x_4*. Provided in Fig. 9 are convergence metrics for the four selected cases. The top row provides the high-fidelity objective function at each OSM iteration, while the bottom row shows the three active constraints: internal volume, planform area, and bending moment coefficient (as defined by the aforementioned constraint functions).
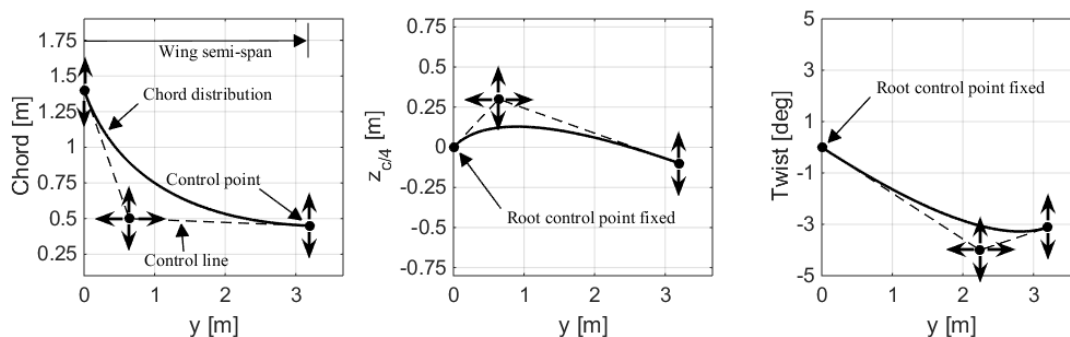

Figure 8. Wing shape distributions for Benchmark Case 6.

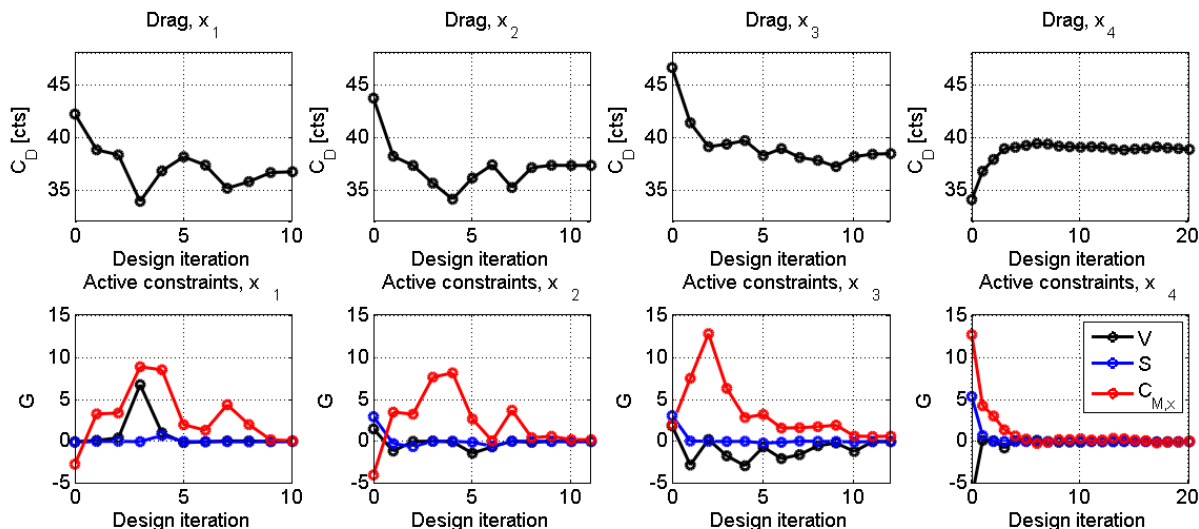American Institute of Aeronautics and Astronautics

Figure 9. Convergence histories of the optimization runs. The upper row of graphs shows drag versus design iteration. The lower row shows the active constraint values versus design iterations. Active constraints include only the internal volume (black), planform area (blue), and bending moment (red), as angle of attack remained well within the allowed range, and thickness was not constrained because the sectional shape was fixed as the NACA 0012 airfoil.

Based on these results, the bending moment constraint appears to be the most difficult to enforce. This is most likely due to the VLM model's method of computing the bending moment coefficient, which involves integration of the span loading. Evidently, this method causes the high- and low-fidelity bending moment coefficient to be poorly correlated in this design space, which is an issue that OSM is unable to correct. This conclusion was further enforced by running the case without the bending moment constraint, which leads to much smoother convergence (as well as a greatly increased drag reduction of 12-13 counts). Furthermore, the high- and low-fidelity drag coefficient may also be poorly correlated near x_4^*, which may have caused poor convergence characteristics.

Shown in Fig. 10 are drag reduction values during the optimization process. Shown on the x-axis is equivalent high-fidelity function evaluations, which is computed based on the number of high- and low-fidelity evaluations, as well as the average time ratio between the VLM and Euler models. In three out of four cases, the optimization process required under 20 equivalent high-fidelity model evaluations, which each required 20-30 minutes when running on 32 processors. Shown on the y-axis is the drag reduction in drag counts, which shows values ranging from 2 to 4 drag counts.
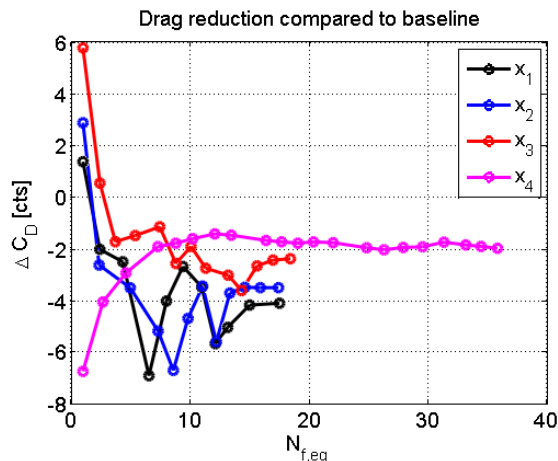

Figure 10. Relative drag reduction (compared to the baseline design) versus optimization computational cost in terms of equivalent high-fidelity evaluations (computed based on number of high- and low-fidelity evaluations, as well as the average time ratio between the models).

10
American Institute of Aeronautics and Astronautics

Table 3 provides an optimization cost summary for the four cases. In most cases, the optimization required 12 or 13 CFD simulations. However, starting from $\mathbf{x_4}$ led to the maximum number of iterations, at which point the optimization was halted. Meanwhile, the other cases stopped due to the step size or objective function stopping criteria. In terms of low-fidelity function calls, most cases required 10-20,000 VLM evaluations, which each took roughly a half second on average. This large number of evaluations was most likely incurred because many of the iterations first ran the pattern search algorithm, and then ran fmincon's SQP algorithm after pattern search failed to locate a feasible design. Regardless, the optimization processes typically required 8-12 hours, which is relatively cheap in computational terms when considering adjoint information was not used.

Given in Table 4 are metrics for the baseline and optimized wing designs. While the bending moment, internal volume, and planform area constraints are all active as expected, the angle of attack constraints ($-3° \leq \alpha \leq 6°$) were never active. This may be due to the design space selected, or more specifically, the sectional shape which is fixed as the NACA 0012 airfoil.

Figure 11 presents the baseline and optimized geometries for the four optimization results. For comparison, a separate optimization result, which did not utilize a bending moment constraint, is shown in green. This additional result used the same OSM algorithm and model setup as the other results, and was started from the baseline design. Looking at the left plot, cases $\mathbf{x_1}$ through $\mathbf{x_3}$ all converged to the same chord distribution. Optimization starting from $\mathbf{x_4}$ is not similar to the others, as it is narrowest in the center of the wing and has a smaller span. However, as mentioned previously, this case is most likely not converged, which may be due to the VLM model's higher error in this region of the design space. The center plot shows the z-coordinate distribution of the quarter-chord line, which seems to show more multi-modality than chord or twist. In particular, $\mathbf{x_1}^*$ and $\mathbf{x_2}^*$ have dihedral in the inboard region and anhedral in the outboard region, while $\mathbf{x_3}^*$ and $\mathbf{x_4}^*$ have the opposite relationship. In terms of twist, all distributions are similar in that they twist downwards close to the wing tip. However, the ones with anhedral in the inboard region ($\mathbf{x_3}^*$ and $\mathbf{x_4}^*$) have higher twist close to the root. Meanwhile, the result without the bending moment constraint is nearly linear with negative tip twist, which is intuitive as it would seem to reduce drag while also having a higher bending moment.

Table 3. Optimization cost metrics for Benchmark Case 6 using Euler & VLM.

	$\mathbf{x_1}$	$\mathbf{x_2}$	$\mathbf{x_3}$	$\mathbf{x_4}$
N_f	12	12	13	21
N_c	18,403	18,967	14,145	37,752
$N_{f,eq}$	17.48	17.40	18.40	35.76
t_c (hr)	2.95	3.27	2.43	5.35
t_f (hr)	6.46	7.27	5.86	7.61
t_{tot} (hr)	9.41	10.54	8.29	12.96
Stopping criterion	Step size	Objective function	Step size	Number of iterations

Table 4. Performance of the baseline and optimized designs for Benchmark Case 6 using Euler & VLM.

	Baseline	$\mathbf{x_1}^*$	$\mathbf{x_2}^*$	$\mathbf{x_3}^*$	$\mathbf{x_4}^*$
C_D (cts)	40.78	36.69	37.29	38.40	38.87
C_{Mx}	0.11369	0.10698	0.10711	0.10754	0.10682
V (m^3)	0.24818	0.24818	0.24824	0.24826	0.24828
S (m^2)	3.0411	3.0710	3.0713	3.0711	3.0700
α (deg)	3.0532	3.1578	3.2229	2.3794	3.1308
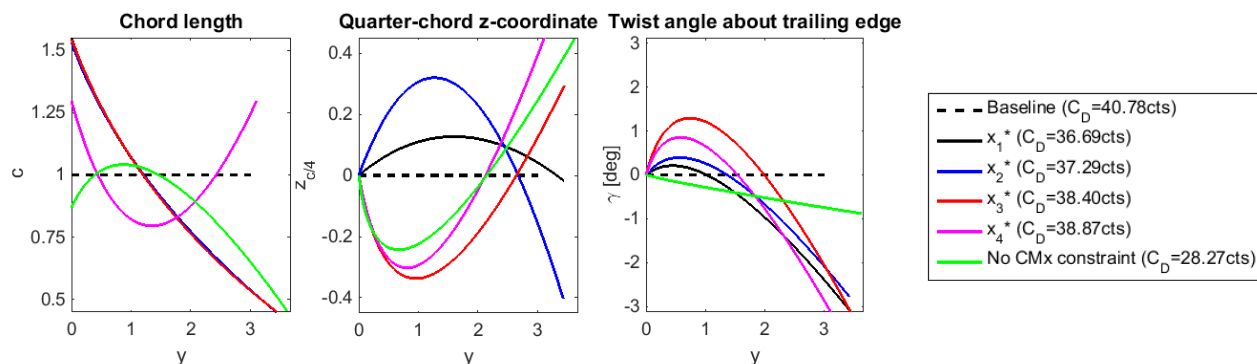
Figure 11. Shape distributions of the baseline and optimized designs for Benchmark Case 6 (Euler & VLM).

American Institute of Aeronautics and Astronautics

It is difficult to quantify how well the VLM-based low-fidelity model matches the Euler design space. Moreover, the unreliable optimization convergence from x_4 is indicative of poor model correlation in some regions of the design space. This appears to be truer for bending moment than for drag. For this reason, we restarted the OSM optimization from the four resulting designs (x_1 through x_4), this time using variable mesh resolution rather than different physics.

Figure 12 shows the resulting convergence histories of the restarted optimization, while Fig. 13 shows the convergence of drag reduction. The first column in Fig. 12 shows relatively uneventful convergence, although the constraints converged to slightly less infeasible values. This suggests that both low-fidelity models (and presumably, the high-fidelity model) have local minima at this design. The second and third columns show different stories, with the drag decreasing significantly during the restarted optimization. This could be indicative of VLM's shortcomings (i.e., its inability to closely match Euler). Alternatively, the coarse-mesh low-fidelity model may lack the necessary resolution to predict dominant trends in the high-fidelity model. Finally, optimization from x_4 was again stopped prematurely, as it was requiring a large amount of time to escape that particular region of the design space.

In terms of constraints, the bending moment constraint now oscillates much less, which was expected. This suggests that, regarding bending moment, the coarse-mesh Euler simulation more closely matches the trends in the high-fidelity model when compared to VLM.
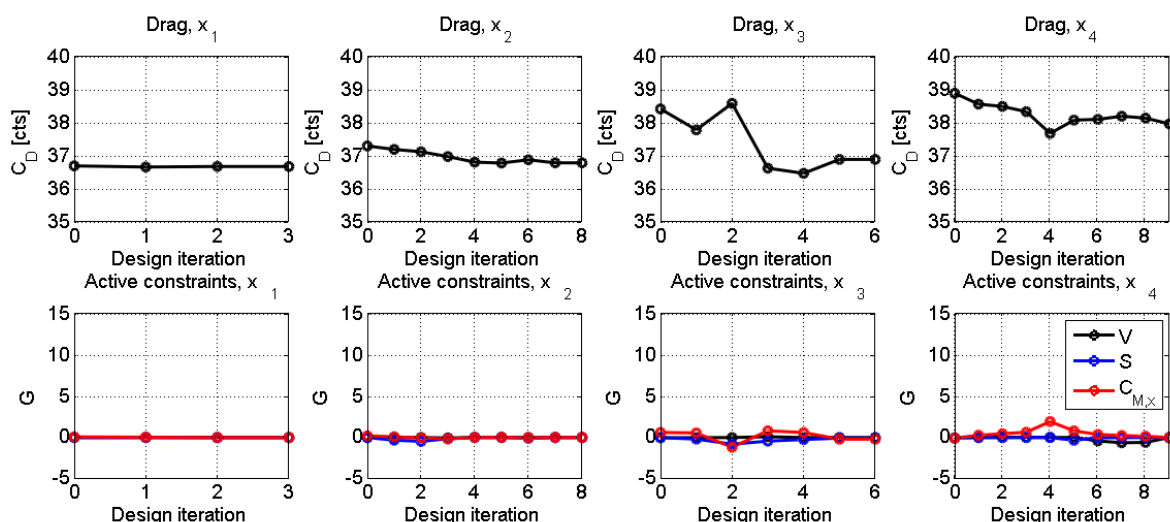

Figure 12. Convergence histories of the optimization runs. The upper row of graphs shows drag versus design iteration. The lower row shows the active constraint values versus design iterations. Active constraints include only the internal volume (black), planform area (blue), and bending moment (red), as angle of attack remained well within the allowed range, and thickness was not constrained because the sectional shape was fixed as the NACA 0012 airfoil.
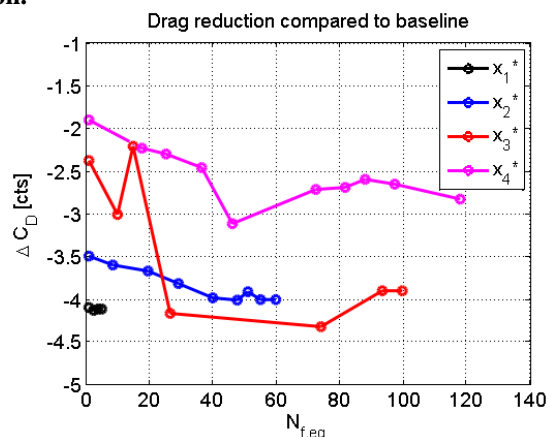

Figure 13. Relative drag reduction (compared to the baseline design) versus optimization computational cost in terms of equivalent high-fidelity evaluations (computed based on number of high- and low-fidelity evaluations, as well as the average time ratio between the models).

12
American Institute of Aeronautics and Astronautics

Tables 5 and 6 show the resulting cost metrics and design performance metrics, respectively. In terms of computational cost, this restarted approach required 2-5 times more computing time than the previous approach. However, both of these approaches were distributed on 4 high-performance computing (HPC) jobs on 32 processors, so this additional step increased the total required time from roughly 2-3 days to 3-5 days.

Figure 14 shows the resulting geometries of the optimized designs. Chord distributions still appear very similar among the designs, excluding the fourth starting point which was stopped prematurely. Conversely, dihedral now varies much less when compared to the previous results. This may suggest that, when dihedral is varied, the VLM model's prediction of drag or bending moment does not closely match the Euler design space. Alternatively, this could also mean that the coarse-mesh Euler model is simply too coarse to capture subtle trends in the high-fidelity design space.

Provided in Figs. 15, 16, 17, and 18 are the initial and final optimized wing shapes, as well as corresponding pressure coefficient contours. In each figure, the left two subplots show the initial design (x_1, x_2, x_3, or x_4) from the LHS sampling plan, while the right two subplots show the optimized shape (x_1^*, x_2^*, x_3^*, or x_4^*). In addition, the top subplots show the wing shapes when viewed from the trailing edge, while the bottom ones show the top surfaces of the wings.

Figure 19 shows a comparison of the baseline and optimized wing shapes when viewed from the trailing edge. In addition, the final drag values are shown as well. It is worth noting that x_1^* (show in black) has both the lowest drag and the lowest variation in dihedral.

Finally, Fig. 20 shows the resulting span loading of the baseline and optimized designs. It is interesting to note that the optimized designs have span load distributions that are nearly linear. This is to be expected, as the bending moment constraint necessitates higher inboard loading when compared to the baseline design. In addition, although x_4^* differs significantly from the other designs, the loading still matches closely with the other optimized designs.

Table 5. Optimization cost metrics for Benchmark Case 6, restarted using Euler (coarse & fine meshes).

	x_1	x_2	x_3	x_4
N_f	4	9	7	10
N_c	545	1,344	2,264	2,104
$N_{f,eq}$	5.05	59.75	99.50	117.68
t_c (hr)	0.51	23.39	43.79	38.95
t_f (hr)	1.93	4.15	3.31	3.62
t_{tot} (hr)	2.44	27.54	47.10	42.57
Stopping criterion	Step size	Step size	Step size	Not converged

Table 6. Performance of the baseline and optimized designs for Benchmark Case 6, restarted using Euler coarse & fine meshes.

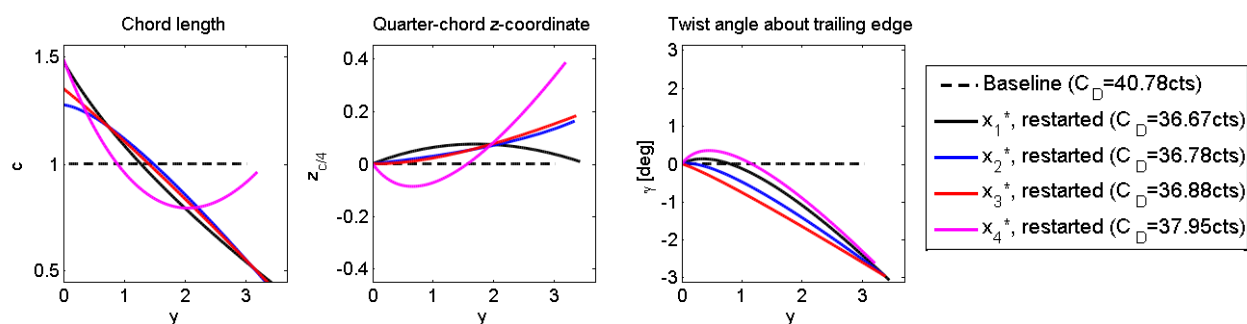|	Baseline	x_1^*	x_2^*	x_3^*	x_4^*
C_D (cts)	40.78	36.67	36.78	36.88	37.95
C_{Mx}	0.11369	0.10689	0.10691	0.10668	0.10690
V (m^3)	0.24818	0.24818	0.24818	0.24819	0.24818
S (m^2)	3.0411	3.0707	3.0709	3.0690	3.0694
α (deg)	3.0532	3.4597	3.6787	3.8690	3.2889

Figure 14. Shape distributions of the baseline and optimized designs for Benchmark Case 6 (Euler & VLM).
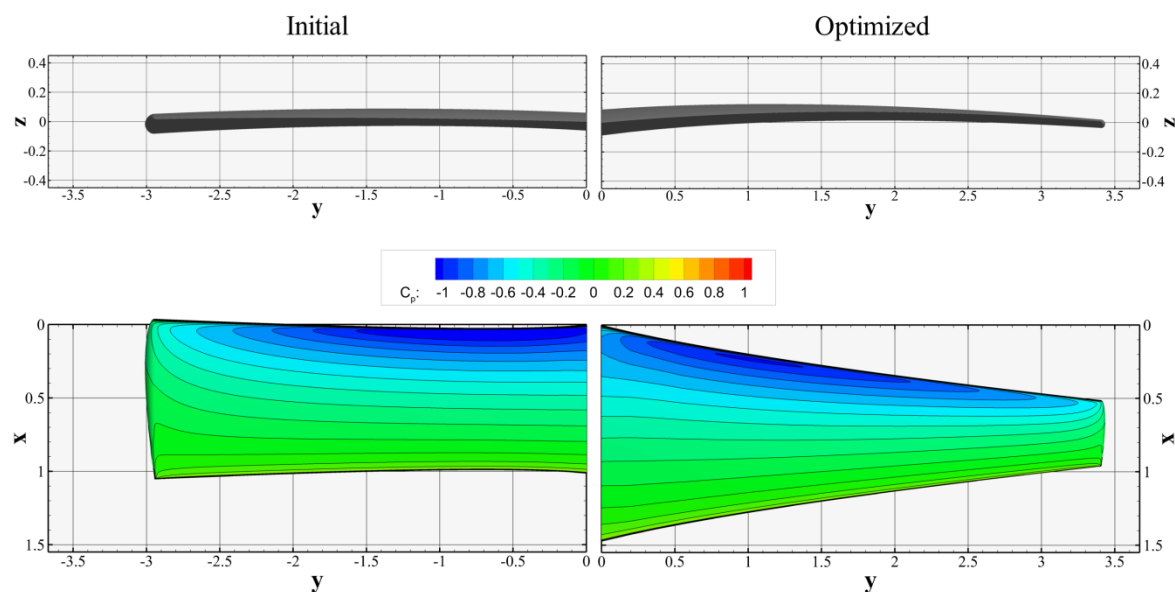
13

Figure 15. Benchmark Case 6 optimized design 1 (x_1): Initial (left) and optimized (right) shapes and surface pressure contours. The upper row shows the trailing edge view, and the lower row shows the planform view.
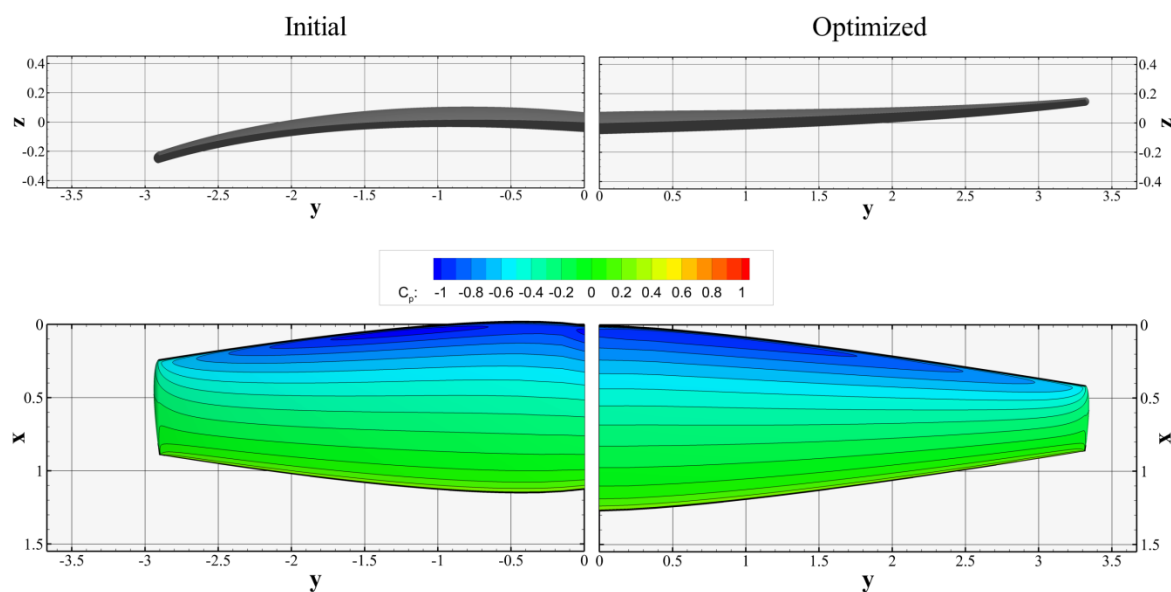

Figure 16. Benchmark Case 6 optimized design 2 (x_2): Initial (left) and optimized (right) shapes and surface pressure contours. The upper row shows the trailing edge view, and the lower row shows the planform view.
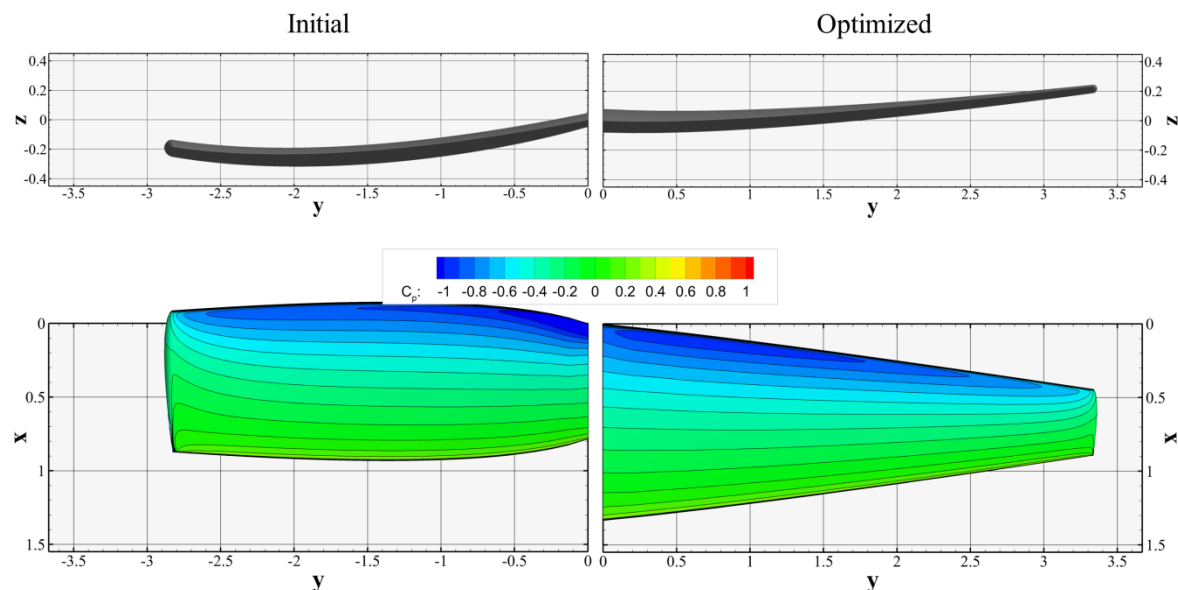
Initial   Optimized

Figure 17. Benchmark Case 6 optimized design 3 (x_3): Initial (left) and optimized (right) shapes and surface pressure contours. The upper row shows the trailing edge view, and the lower row shows the planform view.

Initial   Optimized

Figure 18. Benchmark Case 6 optimized design 4 (x_4): Initial (left) and optimized (right) shapes and surface pressure contours. The upper row shows the trailing edge view, and the lower row shows the planform view.
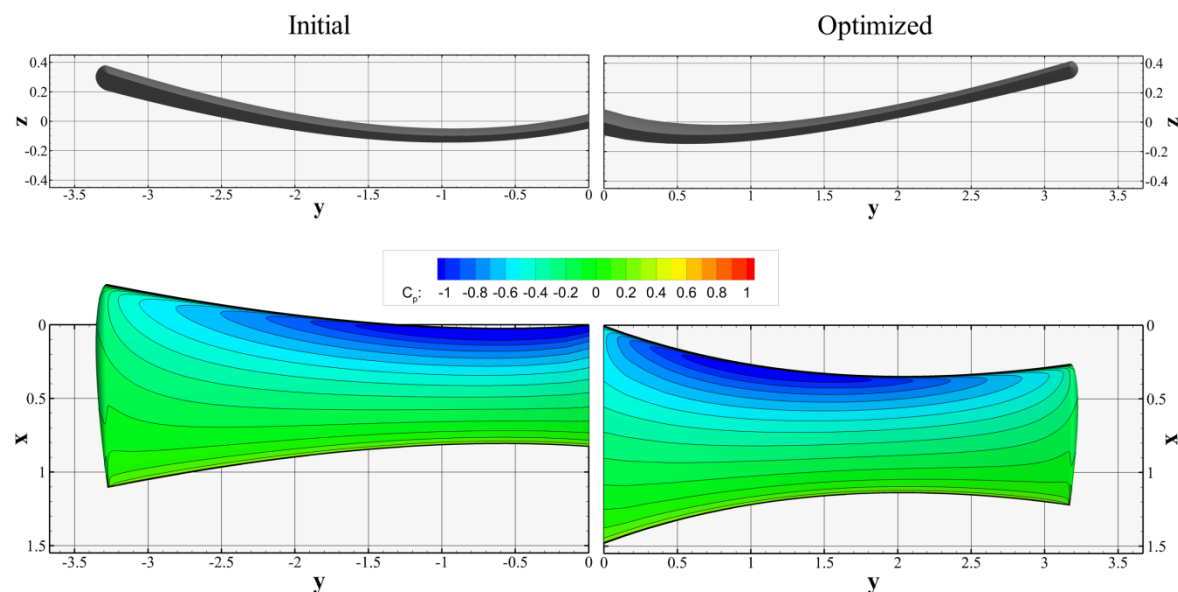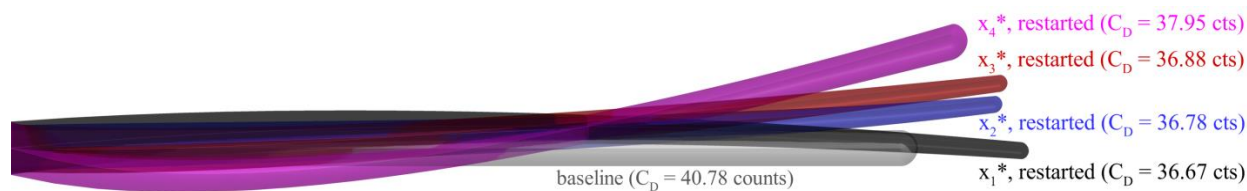

x_4*, restarted (C_D = 37.95 cts)
x_3*, restarted (C_D = 36.88 cts)
x_2*, restarted (C_D = 36.78 cts)
x_1*, restarted (C_D = 36.67 cts)
baseline (C_D = 40.78 counts)

Figure 19. Trailing edge view of the baseline shape and all the optimized wing shapes

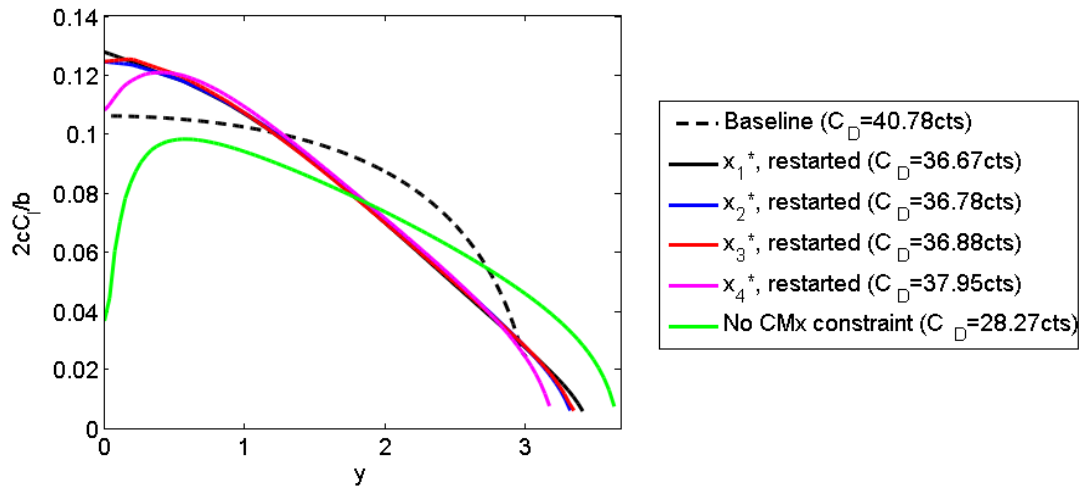American Institute of Aeronautics and Astronautics

Figure 20. Span loading of the baseline and the optimized designs.

IV. Conclusion

Two benchmark aerodynamic design cases involving lift-constrained drag minimization of an unswept and untwisted rectangular wing in subsonic inviscid flow have been solved using surrogate-based optimization (SBO) techniques. In the first case (Benchmark Case 3), the optimization algorithms, both local and global search, were able to recover the ideal (elliptical) lift distribution as anticipated, although the computational cost of the algorithms varied significantly. In the second case (Benchmark Case 6), the multi-start local SBO algorithm converged to several local minima, indicating that the design space is multimodal in that case. However, further investigations are required since the lower fidelity model utilized in the study can be inaccurate under certain circumstances. Future work in this case will include global search with the high-fidelity model to verify and investigate the multimodality of the design space.

References

[1]Leifsson, L., Koziel, S., Tesfahunegn, Y.A., Hosder, S., and Gramanzini, J.-R., "Aerodynamic Design Optimization: Physics-based Surrogate Approaches for Airfoil and Wing Design," *AIAA 52nd Aerospace Sciences Meeting*, National Harbor, Maryland, January 13-17, 2014.

[2]Tesfahunegn, Y.A., Koziel, A., Gramanzini, J.-R., Hosder, S., Han, Z.-H., and Leifsson, L., "Direct and surrogate-based optimization of benchmark aerodynamic problems: A Comparative Study," *53rd AIAA Aerospace Sciences Meeting, Science and Technology Forum*, Kissimee, Florida, Jan 5-9, 2015.

[3]A.I.J. Forrester and A.J. Keane, "Recent advances in surrogate-based optimization," *Prog. in Aerospace Sciences*, vol. 45, no. 1-3, pp. 50-79, Jan.-April, 2009.

[4]Han, Z.-H., "Improving Adjoint-based Aerodynamic Optimization via Gradient- Enhanced Kriging," AIAA-2012-0670, 2012.

[5]S. Koziel, D. Echeverría-Ciaurri, and L. Leifsson, "Surrogate-based methods," in S. Koziel and X.S. Yang (Eds.) *Computational Optimization, Methods and Algorithms*, Series: Studies in Computational Intelligence, Springer-Verlag, pp. 33-60, 2011.

[6]Koziel, S., and Leifsson, L., "Knowledge-based airfoil shape optimization using space mapping," AIAA Paper 2012-3016, 30th *AIAA Applied Aerodynamics Conference*, New Orleans, Louisiana, June 25-28, 2012.

[7]Koziel, S., and Leifsson, L., "Multi-Level Surrogate-Based Airfoil Shape Optimization," 51st *AIAA Aerospace Sciences Meeting including the New Horizons Forum and Aerospace Exposition*, Grapevine, Texas, January 7-10, 2013.

[8]Palacios, F., Colonno, M. R., Aranake, A. C., Campos, A., Copeland, S. R., Economon, T. D., Lonkar, A. K., Lukaczyk, T. W., Taylor, T. W. R., and Alonso, J. J., *"Stanford University Unstructured (SU²): An open-source integrated computational environment for multi-physics simulation and design," AIAA Paper 2013-0287*, 51st *AIAA Aerospace Sciences Meeting and Exhibit*, Grapevine, Texas, USA, 2013.

[9]Ren, Z., Thelen, A. S., Amrit, A., Du, X., Leifsson, L., Tesfahunegn, Y.A., Koziel, S., "Application of Multifidelity Optimization Techniques to Benchmark Aerodynamic Design Problems", *54th AIAA Aerospace Sciences Meeting*, San Diego, California, USA.

[10]Jameson, A., "Aerodynamic Design via Control Theory," *Journal of Scientific Computing*, Vol. 3, 1988, pp. 233-260.

[11]Jones, D.R., Schonlau, M., Welch, W.J., "Efficient global optimization of expensive black-box functions," *Journal oGlobal Optimization,* Vol. 13, No. 4, 1998, pp. 455-492.

[12]Giunta, A.A., Wojtkiewicz, S.F., Eldred, M.S., "Overview of modern design of experiments methods for computational simulations," AIAA-2003-649, 2003.

[13]Han, Z.-H., "SurroOpt: a generic surrogate-based optimization code for aerodynamic and multidisciplinary design," 30th congress of the international council of the aeronautical sciences, Korea, 2016.

[14]Han, Z.-H., Goertz, S., Zimmermann, R. "Improving variable-fidelity surrogate modeling via gradient-enhanced kriging and a generalized hybrid bridge function," *Aerospace Science and Technology*, Vol. 25, 2013, pp. 177-189.

[15]Han, Z. -H., Zimmermann, R., and Goertz, S., "an Alternative Cokriging Model for Variable-Fidelity Surrogate Modeling," *AIAA Journal,* Vol. 50, No. 5, 2012, pp. 1205-1210.

[16]Han, Z. -H., and Goertz, S., "Hierarchical Kriging Model for Variable-Fidelity Surrogate Modeling," *AIAA Journal,* Vol. 50, No. 5, 2012, pp. 1285-1296.

[17]Liu, J., Song, W. -P., Han, Z. -H., and Zhang, Y., "Efficient Aerodynamic Shape Optimization of Transonic Wings Using a Parallel Infilling Strategy and Surrogate Models," *Structural and Multidisciplinary Optimization*, Vol. 55, 2017, pp. 925-943.

[18]Forrester, A., Sobester, A., Keane, A., *Engineering Design via Surrogate Modelling: A Practical Guide*, Wiley, 2008.

[19]Roy, C., "Grid Convergence Error Analysis for Mixed-Order Numerical Schemes," *AIAA Journal*, Vol. 41, No. 4, 2003, pp. 595-604.